Molecular cloud formation by compression of magnetized turbulent gas subjected to radiative cooling

Ankush Mandal [●],[1,2]★ Christoph Federrath[1]★ and Bastian Körtgen [●][3]

[1]*Research School of Astronomy & Astrophysics, The Australian National University, Canberra, ACT, Australia*
[2]*Inter-University Centre for Astronomy and Astrophysics, Pune 411007, India*
[3]*Hamburger Sternwarte, Universität Hamburg, Gojenbergsweg 112, D-21029 Hamburg, Germany*

ABSTRACT

Complex turbulent motions of magnetized gas are ubiquitous in the interstellar medium (ISM). The source of this turbulence, however, is still poorly understood. Previous work suggests that compression caused by supernova shockwaves, gravity, or cloud collisions, may drive the turbulence to some extent. In this work, we present three-dimensional (3D) magnetohydrodynamic (MHD) simulations of contraction in turbulent, magnetized clouds from the warm neutral medium of the ISM to the formation of cold dense molecular clouds, including radiative heating and cooling. We study different contraction rates and find that observed molecular cloud properties, such as the temperature, density, Mach number, and magnetic field strength, and their respective scaling relations, are best reproduced when the contraction rate equals the turbulent turnover rate. In contrast, if the contraction rate is significantly larger (smaller) than the turnover rate, the compression drives too much (too little) turbulence, producing unrealistic cloud properties. We find that the density probability distribution function evolves from a double lognormal representing the two-phase ISM, to a skewed, single lognormal in the dense, cold phase. For purely hydrodynamical simulations, we find that the effective driving parameter of contracting cloud turbulence is natural to mildly compressive ($b \sim 0.4$–0.5), while for MHD turbulence, we find $b \sim 0.3$–0.4, i.e. solenoidal to naturally mixed. Overall, the physical properties of the simulated clouds that contract at a rate equal to the turbulent turnover rate, indicate that large-scale contraction may explain the origin and evolution of turbulence in the ISM.

Key words: magnetohydrodynamics-turbulence – molecular cloud-ISM .

1 INTRODUCTION

Molecular clouds (MCs) – the birthplace of the stars – have been a matter of interest for the last few decades. Extensive studies about the interstellar medium (ISM) and giant molecular clouds (GMC) have established that the gases in the ISM and MCs are highly magnetized and supersonically turbulent in nature. The star formation rate (SFR) in MCs is directly correlated with the physical properties of the clouds. For example, it is a complex competition between supersonic turbulence and self-gravity along with the column density, magnetic field, radiation, and thermal pressure that determines when and where stars form inside the clouds (Mac Low & Klessen 2004; Larson 2005; McKee & Ostriker 2007). However, observations show that the rate of the formation of stars is much slower than that expected if the clouds were forming stars at a free-fall rate (Zuckerman & Evans 1974; Wong &

Blitz 2002; Gao & Solomon 2004). Thus, this indicates that there are physical processes that oppose the gravitational free-fall. The current understanding is that supersonic turbulence plays a crucial role in opposing the fast gravitational collapse (Vázquez-Semadeni, Ballesteros-Paredes & Klessen 2003; Mac Low & Klessen 2004; Federrath & Klessen 2012; Padoan et al. 2014; Krumholz & Federrath 2019). However, it has been established that un-driven supersonic turbulence decays quickly, on a time scale comparable to the turnover time of the largest eddies (Mac Low et al. 1998; Padoan & Nordlund 1999). This means that turbulence must be driven by some physical mechanism (Federrath et al. 2017).

Here we study the maintenance and dissipation of turbulence in MCs in the context of star formation theories. Despite its importance and inevitability for star formation, the origin and evolution of the interstellar medium from the warm atomic phase to the cold, dense MCs is still poorly understood. There are a number of proposed models that act as a source of driving of the turbulence, which include protostellar outflows (Li & Nakamura 2006; Wang et al. 2010; Federrath et al. 2014), feedback from massive stars such

★ E-mail: ankushm@iucaa.in (AM); christoph.federrath@anu.edu.au (CF)

as expanding H II regions (Matzner 2002; Krumholz, Matzner & McKee 2006; Goldbaum et al. 2011), energy injection from ongoing accretion (Klessen & Hennebelle 2010; Vázquez-Semadeni et al. 2010; Lee & Hennebelle 2016), gravitational contraction on small scales (Federrath et al. 2011; Sur et al. 2012) or supernova feedback (Körtgen et al. 2016; Padoan et al. 2016a,b; Pan et al. 2016a).

On the other hand, large-scale contraction of MCs has gained some attention recently in the list of driving agents of the turbulence. Recent numerical and observational studies (Ntormousi et al. 2011; Tremblin et al. 2014; Dawson et al. 2015) show that MCs may be formed at the stagnation point between two expanding superbubbles due to the compression induced by the expansion, even without self-gravity. This motivates us to consider a large-scale global compression (not necessarily due to self-gravity) as a potential agent of driving the turbulence and a mechanism for MC formation as the global compression has the ability to pump energy into the turbulence to slow down the collapse (Körtgen, Federrath & Banerjee 2017; Birnboim, Federrath & Krumholz 2018).

Large-scale contraction in a turbulent medium has been studied for non-magnetized turbulence by Robertson & Goldreich (2012), where they considered the equation of state to be isothermal and the compression can inject energy in a way that they have described as adiabatic heating. Birnboim et al. (2018) studied the same phenomenon, but for isothermal magnetohydrodynamic (MHD) turbulence. In this model, when the gas gets compressed, the velocity increases due to $P - V$ work (there P and V are the pressure and volume of the cloud) against the kinetic pressure (pressure that is generated by the kinetic motions of the particle hitting and rebounding from the surface). Due to compression, the eddy turnover timescale ($\tau \sim L/v$) decreases, and as a result, the dissipation rate increases. Thus, depending on the balance between compression timescale (here parametrized by a negative 'Hubble' parameter, $H = \dot{a}/a$, where a is the time-independent scale factor; see details in the method section) and the dissipation timescale ($\tau = 1/\omega = aL/(2v)$, where ω, L and v are the turnover frequency, cloud size, and velocity dispersion, respectively), the turbulence can get amplified or dissipates away.

However, Robertson & Goldreich (2012) and Birnboim et al. (2018) did not include the effects of radiative heating and cooling, which are crucial for the transition from the atomic to the molecular phase of interstellar clouds. Gas inside the MCs usually radiates its internal energy (radiative cooling) or absorbs energy from the incident radiation (radiative heating) through different complex mechanisms, and the cooling or heating rate depends on various physical parameters that have been studied extensively (Cox & Tucker 1969; Raymond, Cox & Smith 1976; Shull & van Steenberg 1982; Sutherland & Dopita 1993). When the magnetized gas is subjected to rapid radiative cooling, the result is a highly supersonic flow (as the turbulent sonic Mach number is proportional to the inverse of temperature). Thus the effect of cooling has the potential to alter the dynamics of the cloud (Koyama & Inutsuka 2002; Vázquez-Semadeni et al. 2007). Moreover, a model for MC evolution is not complete, if it only predicts the source of the driving of turbulence, but not the formation of the cloud itself. A successful model would also reproduce the physical properties of the clouds that have been measured through different observational techniques (see Heyer & Dame 2015, for a detailed overview and references therein).

From various theoretical models and observational surveys, it has been established that MCs are highly supersonic and magnetized with Mach number ($\mathcal{M}$) $\sim$ 5–20, temperature (T) $\sim$ 10–50 K, density range, $n \sim 10^2$–10^5 cm^{-3} (Wilson, Walker & Thornley 1997;

Hughes et al. 2010). Larson (1981) first pointed out that there is a strong correlation between the velocity dispersion (σ_v) and the size of the cloud (L), and established a scaling relation ($L-\sigma_v$ scaling relation) in the form of a power law, $\sigma_v \propto \ell^{0.5}$ (ℓ is the cloud size in the unit of pc), that has been verified observationally (Solomon et al. 1987; Crutcher 1999; Ossenkopf & Mac Low 2002; Heyer & Brunt 2004; Roman-Duval et al. 2011) . In addition, the magnetic field strength (B) also shows a correlation with the number density of the cloud in the high-density regime, $n \gtrsim 10^3$ cm^{-3} (Crutcher 2012).

In this work, we aim to extend the works by Robertson & Goldreich (2012) and Birnboim et al. (2018). In particular, we seek to determine whether the effects of heating and cooling, which were not included in Robertson & Goldreich (2012) and Birnboim et al. (2018), can change the dynamics and structure of the MCs. To this end, we run three-dimensional (3D) hydrodynamic (HD) and MHD simulations including equilibrium heating and cooling. We consider different compression rates with respect to the eddy turnover rate to figure out the dependence of physical properties of the MCs on the global compression rate, and to determine which contraction model is most favourable in the context of MC formation and evolution by comparing the results from simulations with theoretical models and observational predictions. We organize the paper in the following way. In Section 2, we discuss the detailed methodology of our simulations, the physics of equilibrium cooling and its implementation. In Section 3, we report the results from simulations. In Section 4, we briefly describe the limitations of our study, and in Section 5 we summarize our conclusions.

2 SIMULATION METHODS

2.1 The FLASH code

We use the modified version of the grid-based code FLASH (Fryxell et al. 2000) to solve the three-dimensional (3D), compressible, ideal MHD equations

$$\frac{\partial}{\partial t}\rho + \nabla \cdot (\rho \boldsymbol{v}) = 0, \tag{1}$$

$$\frac{\partial}{\partial t}(\rho \boldsymbol{v}) + \nabla \cdot \left(\rho \boldsymbol{v} \otimes \boldsymbol{v} - \frac{1}{4\pi}\boldsymbol{B} \otimes \boldsymbol{B}\right) + \nabla P_{\text{tot}} = 0, \tag{2}$$

$$\frac{\partial}{\partial t}e + \nabla \cdot \left[(e + P_{\text{tot}})\boldsymbol{v} - \frac{1}{4\pi}(\boldsymbol{B} \cdot \boldsymbol{v})\boldsymbol{B}\right]$$
$$= \frac{1}{\rho}\left[\frac{\rho}{\mu m_{\text{H}}}\Gamma - \left(\frac{\rho}{\mu m_{\text{H}}}\right)^2 \Lambda(T)\right], \tag{3}$$

$$\frac{\partial}{\partial t}\boldsymbol{B} - \nabla \times (\boldsymbol{v} \times \boldsymbol{B}) = 0, \quad \nabla \cdot \boldsymbol{B} = 0. \tag{4}$$

Here, ρ, $\boldsymbol{v}$, $P_{\text{tot}} = P_{\text{th}} + (1/8\pi)|\boldsymbol{B}|^2$, $\boldsymbol{B}$, μ and $e = \rho\epsilon_{\text{int}} + (1/2)\rho|\boldsymbol{v}|^2 + (1/8\pi)|\boldsymbol{B}|^2$ denote the gas density, velocity, total pressure (including thermal and magnetic), magnetic field, mean molecular weight of the particles, and total energy density (internal, kinetic, and magnetic). For simplicity, we assume $\mu = 1$ throughout this study, which does not affect the main conclusions of this study (see Section 4). The MHD equations are closed by the ideal gas equation of state

$$P_{\text{th}} = (\gamma - 1)\rho\epsilon_{\text{int}}, \tag{5}$$

where we assume $\gamma = 5/3$ throughout. The energy equation also includes the heating (Γ) and cooling (Λ) terms, which we discuss in Section 2.3. To solve the system of MHD equations (1)–(4), we use the robust HLL3R Riemann scheme by Waagan, Federrath &

Klingenberg ([2011](#)), based on previous developments in applied mathematics, to maintain positive density and pressure.

2.2 MHD equations in a contracting reference frame

Although the default hydrodynamic scheme in FLASH is written for a static frame of reference, one can use the cosmology module in FLASH to solve the MHD equations in an expanding or contracting frame of reference. In order to do this, we change the MHD equations from the physical coordinate system to the co-moving coordinate system, where additional terms appear due to contraction or expansion. All calculations are assumed to take place in co-moving coordinates $x = r/a$, where r is the physical position vector and x is the co-moving position vector. $a(t)$ is the dimensionless scale factor, which depends on time. The transformation of time and space derivatives in co-moving coordinates is related to the proper coordinates by $(\partial/\partial t)_x = (\partial/\partial t)_r + H r \cdot \nabla_r$ and $\nabla_x = a\nabla_r$, where the Hubble constant (H) is defined as $H = \dot{a}/a$. The physical velocity is $\tilde{v} = Hr + a\dot{x}$, where the first term is the Hubble flow and the second term is called peculiar velocity, i.e. the velocity in the co-moving frame of reference.

The hydrodynamic quantities in the physical (with tilde) and co-moving (without tilde) coordinate system are related by the following equations:

$$\rho = a^3 \tilde{\rho}, \tag{6}$$

$$P_{\text{tot}} = a\tilde{P}_{\text{tot}}, \tag{7}$$

$$e = a\tilde{e}, \tag{8}$$

$$\epsilon_{\text{int}} = a^{-2}\tilde{\epsilon}_{\text{int}}, \tag{9}$$

$$\boldsymbol{B} = a^{1/2}\tilde{\boldsymbol{B}}. \tag{10}$$

The MHD equations in co-moving coordinates can be determined using a definition of a time and space derivative along with prior hydrodynamic quantities, which read

$$\frac{\partial}{\partial t}\rho + \nabla \cdot (\rho \boldsymbol{v}) = 0, \tag{11}$$

$$\frac{\partial}{\partial t}(\rho \boldsymbol{v}) + \nabla \cdot \left(\rho \boldsymbol{v} \otimes \boldsymbol{v} - \frac{1}{4\pi}\boldsymbol{B} \otimes \boldsymbol{B}\right) + \nabla P_{\text{tot}} = -2H\rho \boldsymbol{v}, \tag{12}$$

$$\frac{\partial}{\partial t}e + \nabla \cdot \left[(e + P_{\text{tot}})\boldsymbol{v} - \frac{1}{4\pi}(\boldsymbol{B} \cdot \boldsymbol{v})\boldsymbol{B}\right] =$$
$$-H[(3\gamma - 1)\rho\epsilon_{\text{int}} + 2\rho \boldsymbol{v} \cdot \boldsymbol{v}] + \frac{1}{\rho}\left[\frac{\rho}{\mu m_{\text{H}}}\Gamma - a^{-3}\left(\frac{\rho}{\mu m_{\text{H}}}\right)^2\Lambda(T)\right], \tag{13}$$

$$\frac{\partial}{\partial t}\boldsymbol{B} - \nabla \times (\boldsymbol{v} \times \boldsymbol{B}) = -\frac{3}{2}H\boldsymbol{B}, \quad \nabla \cdot \boldsymbol{B} = 0, \tag{14}$$

where $\partial/\partial t \equiv (\partial/\partial t)_x$ and $\nabla \equiv \nabla_x$ are the derivatives in the co-moving frame. We use operator splitting to account for the Hubble source terms, where the co-moving hydrodynamic variables are modified in each time step to account for the expansion/contraction (Birnboim et al. [2018](#)).

2.3 Radiative heating and cooling

The previous studies by Robertson & Goldreich ([2012](#)) and Birnboim et al. ([2018](#)) used an isothermal equation of state. However, in the real ISM, gas can absorb or emit radiation depending on the quantum state and composition of the gas. There are various

mechanisms that can heat or cool: photoelectric heating from small grains and polycyclic aromatic hydrocarbons, heating and ionization from cosmic rays and X-rays, H_2 formation and destruction, atomic line cooling from hydrogen, etc. (Sutherland & Dopita [1993](#)). As a result, the temperature of the cloud varies, depending on the balance between these various heating and cooling processes. The heating or cooling rate depends on the temperature of the gas cloud, which again depends on the density (ρ). As for static turbulence, the mean density remains constant, the temperature does not vary that much, which means the cooling rate is almost constant throughout the evolution. But, for compressing turbulence, the mean gas density increases with time, and hence, temperature varies a lot. As a result, the heating or cooling rate varies, which has a profound effect on the evolution of the turbulence.

Here we use tabulated values for Γ and Λ developed by Koyama & Inutsuka ([2002](#)) and Vázquez-Semadeni et al. ([2007](#)), based on a constant heating rate

$$\Gamma = 2 \times 10^{-26} \text{ erg s}^{-1}, \tag{15}$$

and a cooling rate based on the following equation:

$$\frac{\Lambda(T)}{\Gamma} = 10^7 \exp\left(\frac{-1.184 \times 10^5}{T + 1000}\right)$$
$$+ 1.4 \times 10^{-2}\sqrt{T}\exp\left(\frac{-92}{T}\right) \text{cm}^3, \tag{16}$$

where the temperature T is in units of Kelvin. These functions are the fits to heating (Γ) and cooling (Λ) due to various processes mentioned above. The thermal equilibrium condition is given by

$$n\Gamma = n^2\Lambda, \tag{17}$$

where $n = \rho/m_{\text{H}}$ is the number density with $\mu = 1$ for this study.

In hydrodynamic simulations, we generally apply cooling by considering the cooling rate in the Courant condition to limit the simulation time step. The densities gradually increase in this problem of gas compression, which means a very small time step can occur as the cooling rate increases. To avoid this problem, we treat cooling as a source term in operator splitting, and following each hydrodynamic step, the internal energy is adjusted. Consider T_{eq} and e_{eq} are the equilibrium temperature and internal energy, and the time required to radiate or absorb excess thermal energy is

$$\tau_\Lambda = \left|\frac{e - e_{\text{eq}}}{n^2\Lambda - n\Gamma}\right|. \tag{18}$$

Let ϵ be the excess energy. The rate of change of energy with time is directly proportional to the instantaneous energy (Newton's cooling law). Thus we have

$$\frac{d\epsilon}{dt} = -\frac{\epsilon}{\tau_{\text{ch}}}. \tag{19}$$

Here τ_{ch} is the characteristic cooling time-scale. Now, if the excess energy after time t is ϵ_1, then

$$\epsilon_1 = \epsilon \exp(-t/\tau_{\text{ch}}). \tag{20}$$

In this case the initial excess internal energy is $\Delta e = e - e_{\text{eq}}$. So, after a time-step dt the excess internal energy will be $\Delta e' = (e - e_{\text{eq}})\exp(-dt/\tau_\Lambda)$. Then we compute the new internal energy e', after a time step dt, as

$$e' = e_{\text{eq}} + (e - e_{\text{eq}})\exp\left(\frac{-dt}{\tau_\Lambda}\right). \tag{21}$$

From this equation, we see that if the gas is undergoing rapid cooling (or heating), $\tau_\Lambda \ll dt$ and $\exp(-dt/\tau_\Lambda) \to 0$, such that the gas

reaches thermal equilibrium very quickly. On the other hand, if the cooling (or heating) rate is very slow, then $\tau_\Lambda \gg \mathrm{d}t$ and equation (21) reduces to

$$e' = e_{\mathrm{eq}} - \mathrm{d}t \, (n^2 \Lambda - n\Gamma). \tag{22}$$

2.4 Initial driving of turbulence to generate initial conditions

As we are experimenting with MHD turbulence statistics in a contracting reference frame, we need a fully developed turbulent field as the initial conditions of the contraction phase. To do that we first drive the turbulence for five eddy turnover times, $\tau = 1/\omega = L/(2\sigma_v)$, on a static background ($a = 1$). Here we consider a box size of $L = 200$ pc, i.e. covering a large portion of the warm neutral ISM with a uniform density of $1\,\mathrm{cm}^{-3}$. We drive turbulence to reach a velocity dispersion $\sigma_v = 10\,\mathrm{km\,s}^{-1}$, typical of the velocity dispersion of the Milky Way on large scales (of order the disc scale height).

The turbulence is driven by applying ρF as a source term in the momentum equation (2). In developing the turbulence acceleration field F, we use the stochastic Ornstein–Uhlenbeck (OU) method (Eswaran & Pope 1988; Schmidt et al. 2009; Price & Federrath 2010). Federrath et al. (2010) developed the code, which is accessible in the public version of FLASH. Turbulent stirring from larger scales is correlated on time-scales related to the lifetime of an eddy on the scale of the simulation domain. The OU process is a well-defined stochastic process with finite autocorrelation time-scale. In our periodic simulation box of side length L, it produces a smoothly varying spatial and temporal driving pattern on the largest scales ($L/2$). The driving process is carried out in Fourier space, and the acceleration field F is set to inject most of the energy into the lowest wave numbers, $1 < |k|L/2\pi < 3$. The spectral shape of the driving field we choose is paraboloid, i.e the peak energy injection is on scale $L/2$, and falls off as a parabola for smaller and higher wavenumber, so that the energy injection at $k = 2\pi/L$ and $k = 6\pi/L$ is identically zero (Federrath et al. 2010; Federrath 2013a, 2016; Birnboim et al. 2018).

Depending on the physical interests, we can build the driving field either purely solenoidal ($\nabla \cdot F = 0$) or compressive ($\nabla \times F = 0$) or a blended field with fractional solenoidal and compressive modes. For separating the driving field into the solenoidal and compressive components, we use the Helmholtz decomposition in Fourier space. For simplicity, we here use only solenoidal driving to develop the turbulence fully before starting the contraction phase ($a < 1$).

2.5 Construction of initial turbulent magnetic field

The interstellar medium is magnetized. Thus, in order to simulate MHD turbulence, we have to set the initial magnetic field. In our study, we chose the magnetic field structure completely random, that is to say, the magnetic field is fully turbulent. In order to construct a fully turbulent magnetic field we use a method that has been considered in the studies of Gerrard, Federrath & Kuruwita (2019) and Birnboim et al. (2018). In this technique, we generate the initial conditions so that all field vectors are randomly oriented, instead of driving the turbulence in the field. We use a Kazantsev power spectrum with an exponent 3/2 to decompose the turbulent field in Fourier space (Brandenburg & Subramanian 2005; Federrath 2016). We restrict the wave vectors in the range $2 < |k|/2\pi < 20$. The Kazantsev spectrum comes from turbulent dynamo amplification (Kazantsev 1968; Federrath et al. 2011) as field amplification works

on the small-scale seeds of the magnetic field (Brandenburg & Subramanian 2005; Schober et al. 2012; Schleicher et al. 2013).

The typical values of the large-scale magnetic field in interstellar clouds in the spiral arms of the Milky Way and also in nearby galaxies are about 3–10 μG (Beck 2015; Han 2017). Therefore, for our MHD simulations we initially set $B = 3$ μG, and after $t = 5\tau$ it has slightly relaxed to $B = 1.8$ μG. Thus, the initial magnetic field is slightly weaker than the observed field, but the MHD simulations nevertheless provide us with at least a reasonable qualitative measurement of MHD effects during cloud contraction.

2.6 Initial conditions, contraction parameters, and list of simulations

All the simulations started from a uniform density $\rho_0 = 1.67 \times 10^{-24}\,\mathrm{g\,cm}^{-3}$ and zero velocities. The simulation box size is initially $L = 200$ pc. Then the turbulence was driven to five eddy turnover times on a static background to establish fully developed turbulence. After that, the driving module has been disabled and the cosmology module has been activated and the evolution followed based on the cosmological factor $a(t)$. The scale factor $a(t)$ of the compression is solely determined by the Hubble parameter (H): $a(t) = \exp[H(t - t_0)]$, where $t \geq t_0$ (t_0 is the contraction start time). In this phase $a(t) < 1$ (Hubble parameter H is negative) as the box started contracting, and the dynamics are determined by the contraction.

In order to study the dependence of the dynamics of turbulent gas on the contraction rate, we chose three values of the Hubble parameter (H): 1. slow compression (the contraction time scale is 10 times longer than the eddy turnover time, $\omega/H = -0.1$), 2. medium compression (contraction time scale is equal to eddy turnover time, $\omega/H = -1$), and 3. fast compression (contraction time scale is 10 times shorter than eddy turnover time, $\omega/H = -10$). Table 1 provides the list of all simulations and initial conditions that have been used for the contraction phase. Fig. 1 shows the evolution of important integrated quantities during the driving phase.

In reality, the large-scale global compression may be induced by various agents, such as supernova explosions, self-gravity, dynamical shocks (from e.g. spiral-arm dynamics), compression induced by ionization fronts, cloud–cloud collisions and many more. Thus, it is not clear what should be the combined compression rate and exact function form caused by all of these mechanisms. Thus, we focus on a simple model of compression, where the compression rate is constant and given in units of the turbulent turnover rate, and we systematically vary this contraction rate over different simulations to study the effect of different contraction rates on the dynamics and cloud properties produced.

Previously, Robertson & Goldreich (2012) and Birnboim et al. (2018) have discussed cases with different contraction rates for pure HD and MHD simulations for isothermal turbulence. Here we are mainly focused on the effect of radiative cooling on contracting background with different contraction rates for pure HD and MHD turbulence in the ISM.

3 RESULTS AND DISCUSSIONS

3.1 Evolution of integrated quantities

In this section we present the main results obtained from our numerical simulations of contracting interstellar clouds that were initialized with the final state shown in Fig. 1. The evolution of important integrated quantities during the contraction phase is shown in Fig. 2 as a function of scale factor (a). The domain size

Table 1. List of different simulation parameters at the beginning of the contraction.

Model	H (s^{-1})	$\tau = 1/\omega$ (s)	ω/H	B (μG)	σ_v (km s^{-1})	$\mathcal{M}$	T (K)	N_{res}^3
HD-Slow	-3.241×10^{-16}	3.08×10^{14}	-0.1	0	11.57	1.85	4.67×10^4	$(512)^3$
HD-Medium	-3.241×10^{-15}	3.08×10^{14}	-1.0	0	11.57	1.85	4.76×10^4	$(512)^3$
HD-Fast	-3.241×10^{-14}	3.08×10^{14}	-10.0	0	11.52	1.84	4.78×10^4	$(512)^3$
MHD-Slow	-3.241×10^{-16}	3.08×10^{14}	-0.1	1.82	11.12	1.75	4.97×10^4	$(512)^3$
MHD-Medium	-3.241×10^{-15}	3.08×10^{14}	-1.0	1.82	11.12	1.75	4.97×10^4	$(512)^3$
MHD-Fast	-3.241×10^{-14}	3.08×10^{14}	-10.0	1.75	11.22	1.75	4.87×10^4	$(512)^3$
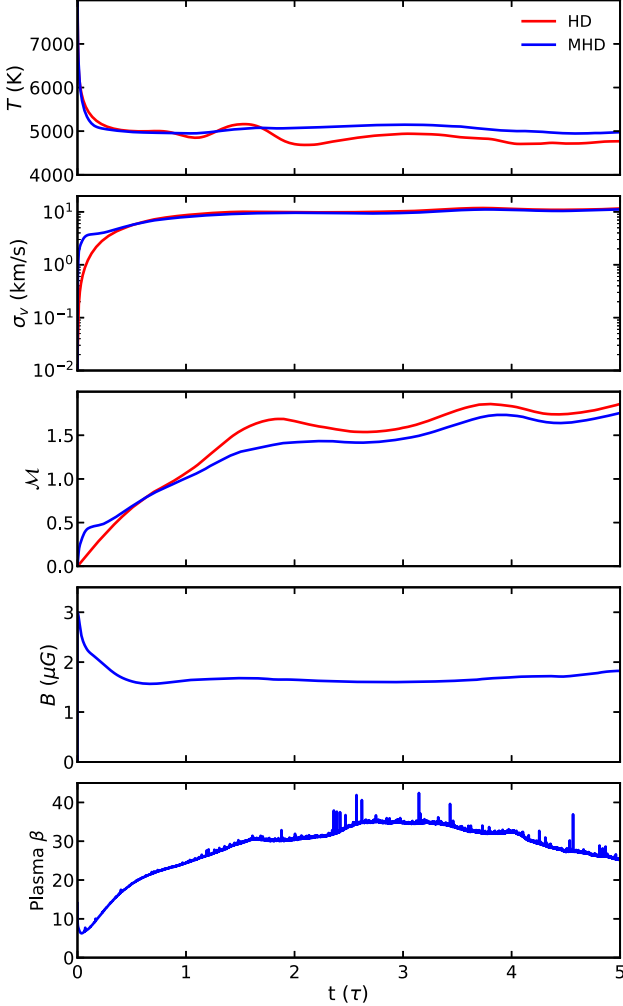
Figure 1. Initial driving phase to establish fully developed turbulence. We take the state at after five eddy turnover times ($t = 5\,\tau$) to serve as the initial condition for the contraction phase. The red line corresponds to the purely HD case and the blue line is for the MHD case.

$L(a) = aL(a = 1)$, such that the cloud has contracted from 200 pc at $a = 1$ down to 2 pc at $a = 0.01$. All the quantities are plotted with decreasing a (on the bottom x-axis) and increasing mean density (on the top x-axis). As the scale factor (a) is exponential in time $a(t) = \exp[H(t - t_0)]$ and the a-axis is in logarithmic scale, it shows the evolution proportional to time. The quantities shown were integrated over the whole volume of the simulation domain. We divide our simulation results in three parts. The first column in Fig. 2 presents the results for slow compression ($\omega/H = -0.1$). The second and third columns correspond to medium ($\omega/H = -1$) and fast ($\omega/H = -10$) compression, respectively. For each case we

consider two types of simulations: 1. a purely HD simulation, and 2. an MHD simulation without guide field.

3.1.1 Evolution of temperature

The first row of Fig. 2 shows the temperature evolution. The initial temperature for all the simulations is approximately the same ($\sim 5000\,$K, the equilibrium temperature of gas with mean density $\sim 1\,$cm^{-3}). As the compression starts the temperature drops. The behaviour of the temperature evolution is similar for each model, because it is primarily determined by the evolution of the mean density, which controls the cooling rate. However, the initial slope of the temperature curve is different for different models. For fast compression the number density grows faster, causing a higher cooling rate and a faster drop in temperature until the density has reached $\sim 10^{-23}\,$g cm^{-3}. Another point to notice is that the presence of a magnetic field does not change the behaviour much, as the HD and MHD simulations for each model follow almost the same temperature evolution. This is expected as (1) the field is weak and does not affect much the density, (2) we do not use a proper heating/cooling via a chemical network, where the species abundances might be affected by the magnetic field. Initially, when the temperature is about $\sim 5000\,$K, the cloud is mostly in the warm atomic phase. As the thermal energy of the particles drops below (due to cooling) the binding energy ($T \sim 150\,$K) of H_2 molecules, the atomic hydrogen undergoes a phase transition to form molecular hydrogen (H_2). From Fig. 2 we find this occurs at $a \sim 0.2$ for slow compression, $a \sim 0.3$ for medium compression, and $a \sim 0.5$ for fast compression. Beyond this epoch, the fraction of molecular H_2 increases gradually and the gas becomes almost fully molecular. When the density $n \sim 10^3$–$10^6\,$cm^{-3}, the temperature drops to ~ 50–$10\,$K and gets saturated around $\sim 10\,$K beyond that. Observations in the Milky Way and extragalactic environments, such as the SMC and LMC, indicate a similar overall temperature dependence on density (Wilson et al. 1997; Bernard et al. 2008; Gratier et al. 2010; Hughes et al. 2010; Heyer & Dame 2015; Jameson et al. 2019). However, there are details in the temperature evolution that clearly depend on the ratio of turbulent turnover rate and contraction rate, which are too subtle to distinguish in observations, based on the temperature evolution alone. Thus, we now turn to more statistics involving the velocity and magnetic field.

3.1.2 Evolution of velocity dispersion (σ_v)

An important distinction between different models is provided by the variation of velocity dispersion (σ_v). The second row of Fig. 2 presents the σ_v evolution with scale factor. Starting from the fully developed turbulence of $\sigma_v \sim 10\,$km s^{-1}, all the simulations start compression, which – depending on the contraction rate – can drive or maintain turbulence to some level. For slow compression ($\omega/H = -0.1$), the compression time-scale is longer than the eddy
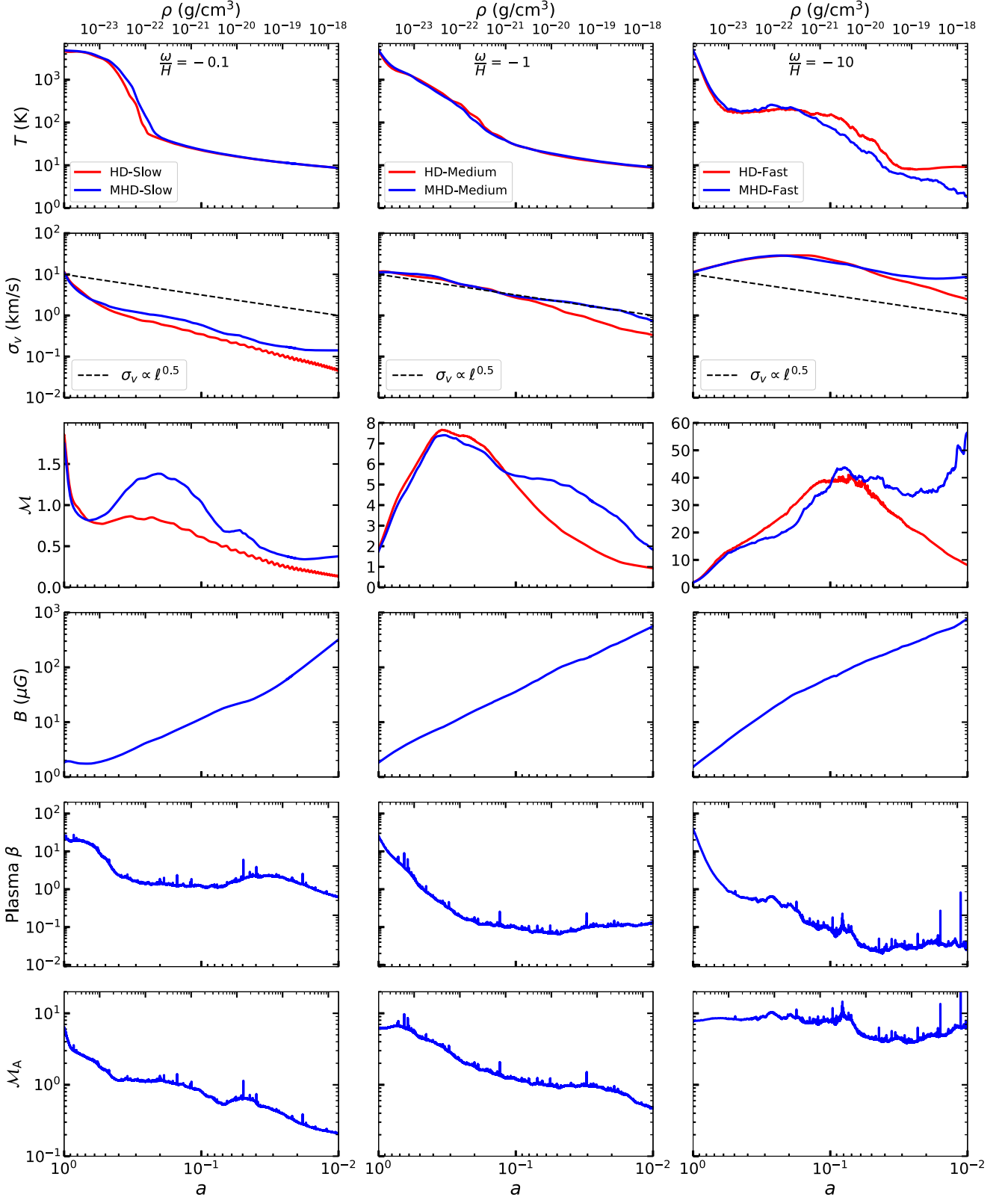
Figure 2. Integrated quantities as a function of scale factor a (bottom axis) and mean density (bottom axis). The different column show (from the left to right) slow ($\omega/H = -0.1$), medium ($\omega/H = -1$), and fast ($\omega/H = -10$) compression. The red lines show the purely HD, and blue lines are for the MHD case. In the velocity dispersion panel (second row) we have plotted the linewidth–size scaling relation (equation 23). Please note the different range of sonic Mach numbers (third row) for the three compression rates.

turnover time-scale. As a result, the dissipation rate dominates over the compression rate and the compression cannot inject energy with enough power to drive the turbulence. Thus, σ_v declines more steeply with a than in the other cases. For fast compression ($\omega/H = -10$), σ_v initially increases and after reaching a peak value it decays with time. This behaviour of increasing to decaying turbulence can be explained by the change of dissipation rate with a. As the dissipation time-scale is proportional to the largest eddy turnover time ($\omega \sim v/2aL$) (Mac Low 1999; Robertson & Goldreich 2012; Birnboim et al. 2018) and a decreases with time, the dissipation time-scale decreases. After some point ($a \sim 0.2$) when ω/H becomes less than -1, the turbulence dissipation dominates.

For medium compression, the compression and dissipation rates are comparable and they remain so for a longer period of time, i.e. the contraction drives just enough turbulence to maintain a nearly constant decline of velocity dispersion with scale, very close to the observed scale dependence of σ_v. We discuss the scaling relation in details in Section 3.2.

3.1.3 Evolution of Mach number ($\mathcal{M}$)

The third row of Fig. 2 shows the evolution of mass-weighted Mach number ($\mathcal{M} = \sigma_v/c_s$) for different simulations. In the cold, dense molecular regime, there is no profound difference between the volume-weighted and mass-weighted Mach number. Here, we chose the mass-weighted Mach number, because it better represents the kinematics in the cold, dense phase, which is where the Mach number may be an important physical quantity to determine the star formation potential of clouds (Federrath & Klessen 2012; Federrath 2013b; Salim, Federrath & Kewley 2015; Sharda et al. 2018, 2019; Beattie, Federrath & Klessen 2019a; Beattie et al. 2019b). The sound speed (c_s) directly depends on the temperature of the cloud ($c_s^2 = \gamma k_B T/\mu m_H$, where γ and μ are the adiabatic index and mean molecular weight of the gas particles, respectively). Initially, for all models, the turbulence is supersonic. Since contraction forces the temperature to drop, the sound speed (c_s) decreases with a, and $\mathcal{M}$ increases, which is a direct consequence of the joint evolution of temperature and velocity. For the medium and fast compression rate, the HD simulations show the same behaviour, i.e $\mathcal{M}$ grows to a peak value and then decays. For slow compression, $\mathcal{M}$ decreases initially, and then grows to a peak value, followed by decay. This behaviour is due to the different rates of change of temperature and velocity dispersion. The interesting point is to notice the behaviour of $\mathcal{M}$ in the MC regime for different compression rates. The typical values of $\mathcal{M}$ in real MCs are known to be supersonic with $\mathcal{M} \sim 5\text{–}20$ (Crutcher 1999; Schleicher et al. 2013). From Fig. 2 we see that the Mach number in the molecular regime for slow compression is subsonic, which is too small. On the other hand, for fast compression, the Mach numbers exceed 30 in the MHD case, which is unusual for Milky Way conditions .[1] Only the simulation

with medium compression rate produces realistic Mach numbers of order 5–10 in the molecular regime and a dependence on scale consistent with the observed velocity dispersion–size relation.

3.1.4 Magnetic field and plasma-β

The fourth row of Fig. 2 shows the magnetic field evolution for the three MHD simulations with different compression rates. For all the simulations, the mean magnetic field ($|\boldsymbol{B}|$) starts from $|\boldsymbol{B}| \approx 2\,\mu\text{G}$ after the initial driving phase (cf. Fig. 1) and starts growing due to the compression of field lines. Observations with different techniques like Zeeman splitting in HI, OH, CN absorption lines (Crutcher et al. 1993; Crutcher 1999; Falgarone et al. 2008), and maser emission from dense MC cores (Vlemmings & van Langevelde 2007; Watson 2009) have shown the existence of magnetic fields in interstellar clouds. All of these studies show that for low-density clouds ($n \lesssim 10^3\,\text{cm}^{-3}$), there is nearly no correlation between the magnetic field strength (B) and the density (ρ). However for dense MCs ($n \gtrsim 10^3\text{–}10^7\,\text{cm}^{-3}$), the magnetic field increases with the density of the cloud (Crutcher 2012). This is usually stated in form of a power law, $|\boldsymbol{B}| \propto \rho^\kappa$. If the cloud undergoes homologous compression, then magnetic flux ($\Phi = \pi R^2|\boldsymbol{B}|$) conservation implies $|\boldsymbol{B}| \propto R^{-2}$, while mass conservation gives $R \propto \rho^{1/3}$; therefore $|\boldsymbol{B}| \propto \rho^{2/3}$. On the other hand, if the magnetic field is strong, the structure of the cloud will be changed by the magnetic field. Fiedler & Mouschovias (1993) numerically showed that for ambipolar diffusion driven contraction $\kappa \approx 0.47$, which has also been seen observationally (Crutcher 1999). However, Basu (2000) showed that a better correlation was obtained by fitting $B \propto \sigma_v\sqrt{\rho}$.

The fifth row of Fig. 2 presents the dependence of plasma-β with a. We see that for the MHD, medium-contraction model, the value of β (the plasma β is defined as the ratio between thermal pressure and magnetic pressure) is about 0.1 in the molecular regime (for real MCs the value of β typically lies between 0.1 and 0.3; see Crutcher 2012; Federrath et al. 2016; Krumholz & Federrath 2019), which implies a significant effect of the magnetic field ($\beta < 1$) (Planck Collaboration XXXV 2016). Thus, we expect the value of κ for our numerical experiment is 0.47 rather than 2/3. We explore more about $B - n$ scaling relation and dependence on β in Section 3.2.

3.2 Scaling relations

From various surveys mentioned in Section 3.1.1 it is empirically established that the velocity dispersion (σ_v) in MCs is correlated with the size of the cloud ℓ (Larson 1981; Solomon et al. 1987; Ossenkopf & Mac Low 2002; Heyer & Brunt 2004; Roman-Duval et al. 2011). Early observations predict that σ_v is related with ℓ in a power-law fashion $\sigma_v \propto \ell^\xi$. Larson (1981) first calculated the value of ξ to be 0.38 (Larson relation). However, from various surveys, the most accepted linwidth-Size scaling relation in recent days is given by

$$\sigma_v \propto \ell^{0.5}, \tag{23}$$

where ℓ is the size of the cloud in the unit of pc and the unit of σ_v is km/s. This correlation also is reproduced by various numerical studies (Kritsuk et al. 2007; Schmidt et al. 2009; Federrath et al. 2010; Federrath 2013a). In Fig. 2 we added the scaling relation (equation 23) on top of the $\sigma_v - a$ lines. Only the simulation with medium compression provides a good match to the observed relation. Fig. 3 shows the scaling relation calculated from the medium compression models along with the Larson (1981) relation
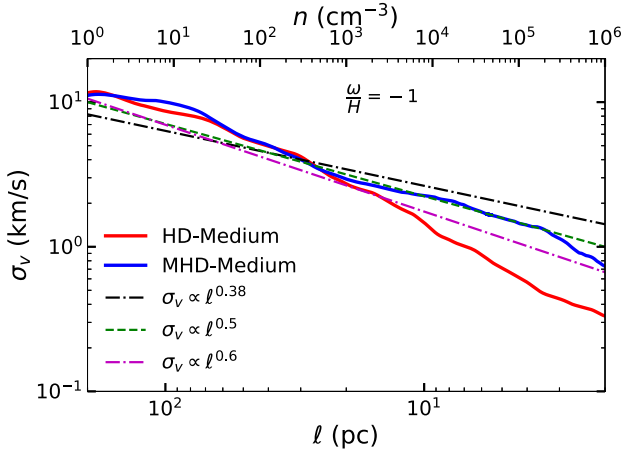
---

[1]For MHD turbulence, the presence of a magnetic field can change the situation considerably. In Fig. 2, we see that the σ_v as well as $\mathcal{M}$ stop decreasing and increases again after a sufficiently long period for MHD simulation in the case of fast compression. Birnboim et al. (2018) have shown that the value of a where the transition from decaying to increasing turbulence happens depends on the presence of the guide field, and the saturation level of turbulent dynamo for isothermal compressive turbulence. The presence of a strong magnetic field changes the flow pattern to nearly dissipationless. An interesting point to note that although Birnboim et al. (2018) pointed out it for isothermal turbulence, the behaviour does not change for the case of turbulence subjected to radiative cooling.

Figure 3. $\ell - \sigma_v$ scaling relation for the simulations with a medium-compression rate ($\omega/H = -1$). The red and blue solid lines correspond to HD and MHD simulations, respectively. The dashed lines are various observational scaling relations. The black dashed line is the $\sigma_v \propto \ell^{0.38}$ Larson (1981) relation. The green and magenta dashed lines are $\sigma_v \propto \ell^{0.5}$ (Solomon et al. 1987) and $\sigma_v \propto \ell^{0.5}$ (Bolatto et al. 2008) linewidth–size scaling relations, respectively.
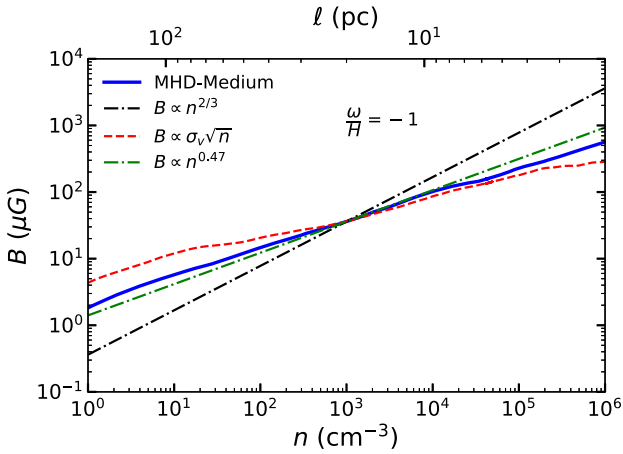
Figure 4. Relation between the magnetic field (B) and the density (n) for the medium-compression simulations ($\omega/H = -1$). The solid blue line corresponds to MHD simulation. The black dashed line presents the scaling relation $|\mathbf{B}| \propto n^{2/3}$ (Crutcher 2012), resulting from homologous collapse of a cloud where the magnetic field is dynamically weak. The green dashed line represents the scaling relation $|\mathbf{B}| \propto n^{0.47}$, established by an ambipolar diffusion driven contraction model (Fiedler & Mouschovias 1993). Finally, the red dashed line shows the scaling relation $B \propto \sigma_v \sqrt{\rho}$ (Basu 2000).

(exponent $\xi = 0.38$), equation (23) and the B08 relation (Bolatto et al. 2008), which has an exponent $\xi = 0.5$. Result shows that the $\ell - \sigma_v$ relation from the medium compression model is consistent with the observational predictions. Moreover, equation (23) fit very well to the MHD model in the molecular regime. This scaling relation is also consistent with the results from MC simulation driven by supernovae including self-gravity (Padoan et al. 2017).

In Fig. 4, we have plotted the dependence of B with number density (n). We adopt the relation in the form of $|\mathbf{B}| = B_0 (n/n_0)^\kappa$ and $|\mathbf{B}| = B_0 (\sigma_v/\sigma_{v,0})(n/n_0)^{0.5}$, where $\kappa = 2/3$ (Crutcher 2012) and 0.47 (Fiedler & Mouschovias 1993) for two different models. Here $n_0 = 10^3$ cm^{-3}, and B_0 and $\sigma_{v,0}$ are the magnetic field and velocity dispersion when the mean number density n_0. As pointed out earlier,

the density–magnetic field correlation is valid in the high-density regime $n \gtrsim 10^3$ cm^{-3}, we choose the starting point of the plots at $n = 10^3$ cm^{-3} and calculate the value of B when $n = 10^3$ cm^{-3} to find the constant B_0. We show the various scaling relations discussed in Section 3.1.4. Since all of these scaling relations are valid only in the high-density regime ($n \sim 10^3$–10^6 cm^{-3}), we expect our simulation results to be consistent with these relations only in the higher density regime. Fig. 4 shows good agreement of the MHD medium-compression model with the theoretical and observational estimates of the $B - n$ relation. As pointed out in Section 3.1.4, $\beta < 1$ implies a significant magnetic influence on the evolution of the cloud, thus κ value will be close to 0.47. Moving-mesh simulations of isothermal, self-gravitating MC cores (Mocz et al. 2017) find $\kappa \approx 1/2$, when the magnetic field is strong ($\beta < 1$), consistent with the simulations presented here. The MHD-Medium compression result approximately follows the $n^{0.47}$ curve. It also fits well to the $\sigma_v \sqrt{n}$ curve in the molecular regime. All of the above results suggest that the $\omega/H = -1$ contraction model produces reasonable cloud parameters as a natural outcome of MC formation by compression out of the warm atomic phase.

3.3 Morphological features

Fig. 5 displays a spatial representation of density (top panel), temperature (middle panel), and Mach number (bottom panel) at $a = 1.0$ (left), $a = 0.1$ (middle), and $a = 0.01$ (right) for the MHD-Medium model. We have plotted the local magnetic field lines projected on to the x–y plane on top of the density projections, and local velocity field vectors in the Mach number projections. In the density projections, we see that initially ($a = 1$), the large-scale turbulence driving sets the density contrasts ranging over one order of magnitude and the local magnetic fields are quite random. However, at a later times ($a = 0.1$ and 0.01), when the strength of the magnetic fields increase, the density contrasts decrease (ranging over a factor of 3). This is because magnetic fields reduce the density contrasts, due to additional magnetic pressure parameterized by the plasma-β (Federrath & Klessen 2012; Molina et al. 2012). The magnetic field directions at this epoch are more regular, which is consistent with the strong-field predictions, i.e. for a strong field, the field lines should be smoother (Crutcher 2012). The temperature (second row in Fig. 5) also shows similar behaviour. Initially ($a = 1$), the temperature fluctuations cover almost four orders of magnitude, while at $a = 0.01$, the temperature fluctuations are very small and gas is nearly isothermal at $T \sim 5$–10 K.

One interesting point to notice is the correlation between density and temperatures. In Fig. 5, we see that the correlations are very prominent. Higher densities have lower temperature as expected due to cooling. The correlations between density and Mach number are quite weak. However, Fig. 5 shows that high-density regions exhibit a lower Mach number on average, as a result of the velocity dispersion–size relation discussed above.

3.4 Density dispersion–Mach number relation

In supersonic, isothermal turbulence, the density fluctuations approximately follow a lognormal distribution (Vazquez-Semadeni 1994), assuming that the local density fluctuations and velocities are uncorrelated (Passot & Vázquez-Semadeni 1998; Federrath et al. 2010; Federrath & Banerjee 2015a; Kritsuk, Ustyugov & Norman 2017). However, if the gas is not isothermal, we do not expect a lognormal distribution for density fluctuations, as the local density and Mach number are correlated (Passot & Vázquez-Semadeni
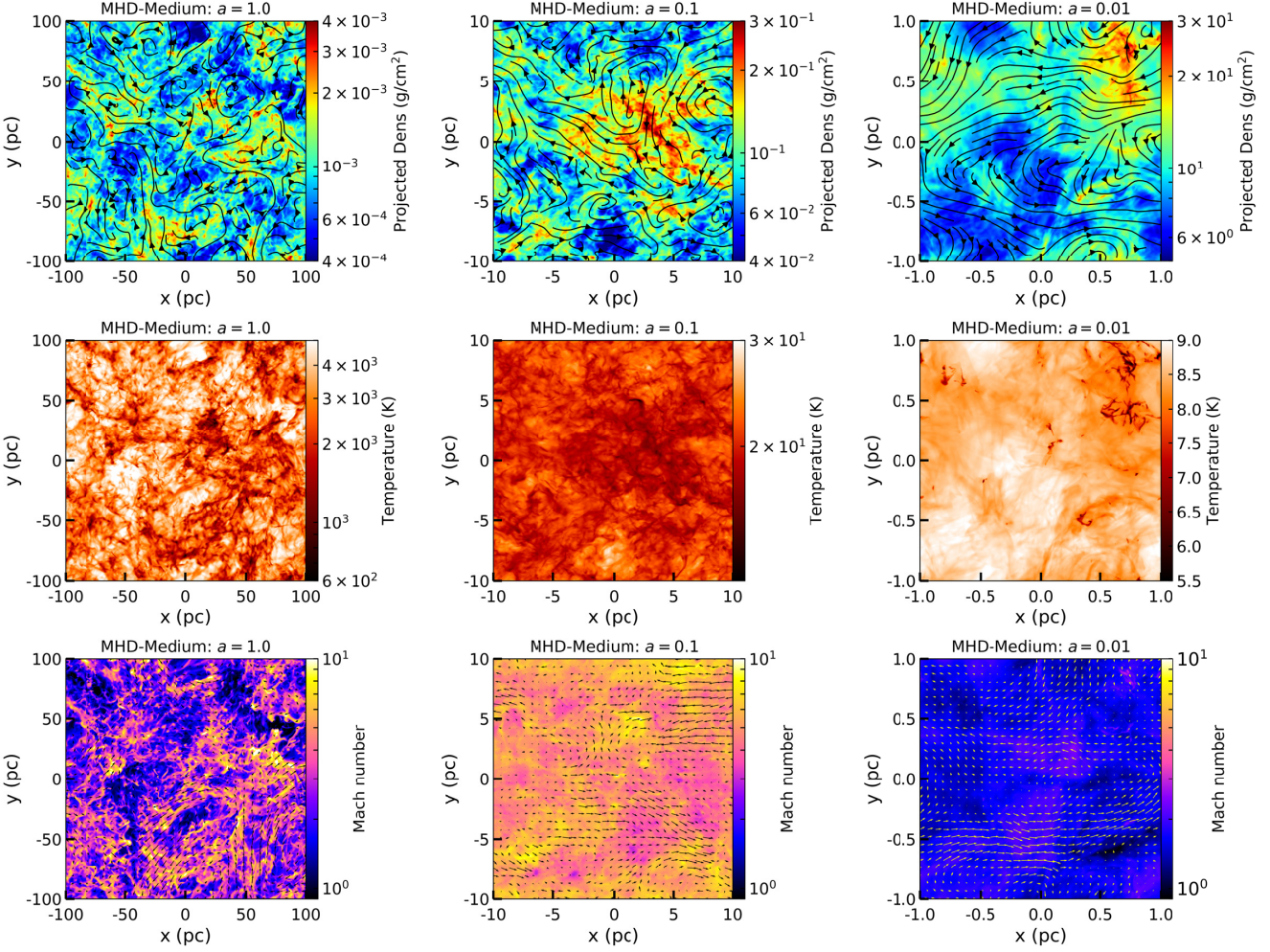
Figure 5. The first row shows the projected density in the *x–y* plane for the MHD-Medium simulation. The second and third rows represent the line-of-sight, density-weighted mean temperature and Mach number, respectively. The first, second, and third columns correspond to *a* = 1.0, 0.1, and 0.01, respectively. The streamlines in the density projections represent the projected magnetic field in the *x–y* plane. The velocity field is shown as arrows in the Mach number projections (bottom panels).

1998; Gazol & Kim 2013; Körtgen, Federrath & Banerjee 2019). Various theoretical and numerical studies (Padoan, Nordlund & Jones 1997a; Passot & Vázquez-Semadeni 1998; Kowal, Lazarian & Beresnyak 2007; Federrath, Klessen & Schmidt 2008) have established that the density dispersion and Mach number follow the relation

$$\sigma_s(b, \mathcal{M}) = \left[\ln(1 + b^2 \mathcal{M}^2)\right]^{1/2}, \tag{24}$$

where σ_s is the variance of the logarithmic density contrast, $s = \ln(\rho/\langle\rho\rangle)$. Federrath et al. (2008, 2010) pointed out that the parameter b is a function of how the turbulence is driven and found $b \approx 1/3$ for purely solenoidal (divergence-free) driving and $b \approx 1$ for purely compressive (curl-free) driving. For magnetized turbulence the σ_s–$\mathcal{M}$ relation is modified by magnetic pressure and was analytically derived by Padoan & Nordlund (2011) and Molina et al. (2012). For $B \propto \rho^{1/2}$ they find

$$\sigma_s(b, \mathcal{M}, \beta) = \left[\ln\left(1 + b^2 \mathcal{M}^2 \frac{\beta}{\beta + 1}\right)\right]^{1/2}, \tag{25}$$

where β is the ratio of thermal to magnetic pressure (denoted plasma-β) of the magnetized flow. Equation (25) is a more general

form, as we can see in the limit of $\beta \to \infty$ (hydrodynamic limit), equations (25) and (24) are identical.

For given σ_s, $\mathcal{M}$, and β, equation (25) can be used to calculate the effective driving parameter b of the turbulence, i.e.

$$b = \left[\frac{\beta + 1}{\beta \mathcal{M}^2} \left(\exp(\sigma_s^2) - 1\right)\right]^{1/2}. \tag{26}$$

In the limit $\beta \to \infty$, equation (26) gives the effective driving parameter for HD turbulence.

An alternative way of estimating b is to consider the mixture of turbulent modes in the velocity field. For this purpose, Pan et al. (2016b) define the compressive ratio

$$\chi = \langle v_{\text{comp}}^2 \rangle / \langle v_{\text{sol}}^2 \rangle, \tag{27}$$

where $\langle v_{\text{comp}}^2 \rangle$ and $\langle v_{\text{sol}}^2 \rangle$ are the compressive and solenoidal components of the velocity field, respectively. An effective driving parameter (b_χ) can then be defined as

$$b_\chi = \sqrt{\frac{\chi}{1 + \chi}}. \tag{28}$$

The velocity components $\langle v_{\mathrm{comp}}^2 \rangle$ and $\langle v_{\mathrm{sol}}^2 \rangle$ can be determined via a Helmholtz decomposition in Fourier space. Thus, from the velocity power spectra one can determine b_χ using equations (27) and (28). However, b in equation (26) may not be the same as b_χ in equation (28), but Pan et al. (2016b) and Jin et al. (2017) argue and show that they are usually fairly similar.

In Fig. 6 we show σ_s (left-hand panels) and the driving parameter $(b, b_\chi;$ right-hand panels) as a function of a. The top panels represent the evolution for the HD-Medium simulation and the bottom panels show the same for the MHD-Medium simulation. Since in the driving phase (before contraction), the turbulence is driven by a solenoidal acceleration field ($b \sim 1/3$), and contraction acts primarily as a compressive acceleration, the resulting driving during the contraction phase is a mixture of solenoidal and compressive components ($1/3 < b < 1$) (fig. 8; Federrath et al. 2010). For our case, we find that $b \approx 0.4$–0.5 provides a good fit in the case without magnetic fields (HD-Medium in the top panels of Fig. 6). We find that the driving parameter b computed using equation (26) with $\beta \rightarrow \infty$ and b_χ computed from the Helmholtz-decomposed velocity field are in good agreement, with $b_\chi \sim 0.4$, somewhat smaller than $b \sim 0.5$.

In the bottom-left panel of Fig. 6, we show the evolution of σ_s for the MHD-Medium simulation. The turquoise line represents the prediction from the theoretical model in the HD limit (equation 24) with $b = 0.4$, while the green line is for the MHD model with the β-parameter included and $b = 0.5$ (equation 25), for comparison. The bottom-right panel shows the evolution of b and b_χ for the MHD-Medium model. The blue solid line corresponds to b directly computed from equation (26) and the black dash–dotted line is b_χ computed using equation (28). The green dotted line corresponds to the evolution of b calculated using equation (26) with $\beta \rightarrow \infty$.

We see that the MHD model (equation 28) does not provide a good fit to the data and suggests $b > 1$ for $a \lesssim 0.2$. This is because equation (25) breaks down as the Alfvén Mach number drops below ~ 2. Indeed, Molina et al. (2012) have shown that this σ_s–$\mathcal{M}$ relation (equation 25) does not work for $\mathcal{M}_A \lesssim 2$, and in our case, $a \lesssim 0.2$ is when this transition to strongly sub-Alfvénic turbulence occurs (cf. the bottom panel of Fig. 2).

Despite these caveats, we find that using the purely hydrodynamical version of the σ_s–$\mathcal{M}$ relation, as well as b_χ, suggest a driving parameter of ~ 0.3–0.4, with b_χ giving a somewhat lower effective driving parameter close to purely solenoidal or less ($b_\chi \sim 0.2$–0.3) than $b \sim 0.4$ from the HD-version of the σ_s–$\mathcal{M}$ relation.

Overall, these results suggest that contracting MHD turbulence has an effectively solenoidal to naturally mixed driving parameter ($b \sim 0.3$–0.4), while contracting HD turbulence is naturally mixed to slightly compressive ($b \sim 0.4$–0.5).

3.5 The density PDFs for different compression models

As pointed out in Section 3.4, for an idealized isothermal turbulence, the density contrast (ρ/ρ_0) follows an approximately lognormal distribution, a Gaussian distribution in the logarithmic density contrast $s \equiv \ln(\rho/\rho_0)$,

$$p_{\mathrm{LN}}(s) = \frac{1}{\sqrt{2\pi\sigma_s^2}} \exp\left(-\frac{(s - s_0)^2}{2\sigma_s^2}\right). \tag{29}$$

The lognormal PDF contains two parameters: (1) the variance of logarithmic density σ_s and (2) the mean s_0, which is related to the variance by $s_0 = \sigma_s^2/2$ because of mass conservation (Padoan, Jones & Nordlund 1997b; Federrath et al. 2008; Hopkins 2013). Although the lognormal model of the density PDF for isothermal

turbulence is well established, this is not obvious for non-isothermal turbulence. Previous studies show that the PDF tends to depart significantly from the lognormal form given by equation (29), if the gas is non-isothermal (Vazquez-Semadeni 1994; Passot & Vázquez-Semadeni 1998; Wada & Norman 2001; Kritsuk & Norman 2002; Li, Klessen & Mac Low 2003; Audit & Hennebelle 2005; Hennebelle & Audit 2007; Seifried et al. 2011; Molina et al. 2012; Gazol & Kim 2013; Hopkins 2013; Federrath & Banerjee 2015b). A model for capturing the non-lognormality of density fluctuation is the intermittency model presented by Hopkins (2013), physically motivated by the quantized log-Poisson statistics for velocity structure functions $[S_p(\boldsymbol{R}) \equiv \langle\delta v(\boldsymbol{R}^p)\rangle]$ (Dubrulle 1994; She & Waymire 1995). The form of the density PDF in case is (Hopkins 2013; Federrath & Banerjee 2015b)

$$p_{\mathrm{HK}}(s) = I_1\left(2\sqrt{\lambda w(s)}\right) \exp[-(\lambda + w(s))]\sqrt{\frac{\lambda}{\theta^2 w(s)}},$$

$$\lambda \equiv \frac{\sigma_s^2}{2\theta^2}, \quad w(s) \equiv \frac{\lambda}{1 + \theta} - \frac{s}{\theta} \ \ (w \geq 0), \tag{30}$$

where $I_1(x)$ is the first-order *modified Bessel function* of the first kind. Equation (30) contains two parameters: (1) the standard deviation σ_s and (2) the intermittency parameter θ. In the zero-intermittency limit ($\theta \rightarrow 0$), equation (30) simplifies to the lognormal PDF, equation (29).

Hopkins (2013), Federrath (2013a), and Federrath & Banerjee (2015b) showed that this intermittency model for the density PDF fits well to the density PDFs of idealized non-isothermal turbulence simulations with a large range of Mach numbers, magnetic field strengths, and turbulence driving parameters. Thus, here we are motivated to examine whether this also true for our non-isothermal contraction model with radiative heating and cooling.

Fig. 7 shows the density PDFs of $s \equiv \ln(\rho/\rho_0)$ obtained in our simulations with different contraction rate. In the first row of Fig. 7, we show the density distribution at $a = 1$ (i.e. when the turbulence is fully developed and immediately before the contraction starts). The second and third row of Fig. 7 correspond to the density distribution at $a = 0.1$ and 0.01 for different compression models, respectively. Different columns (from *left* to *right*) correspond to MHD-Slow, MHD-Medium, and MHD-Fast compression models. In each panel, the red points are the density PDFs from the simulation data.

At $a = 1$ (top panel in Fig. 7), we see that the density distribution is divided into two phases: (1) diffuse warm gas, and (2) dense cold gas. Thus, natural motivation indicates that each of these phases may follow a separate lognormal distribution. Thus, for the entire density range, we fit a double-lognormal PDF (e.g. Dawson et al. 2015)

$$p_{\mathrm{DLN}}(s) = \frac{N}{\sqrt{2\pi\sigma_{s1}^2}} \exp\left(-\frac{(s - s_{01})^2}{2\sigma_{s1}^2}\right) +$$

$$\frac{1 - N}{\sqrt{2\pi\sigma_{s2}^2}} \exp\left(-\frac{(s - s_{02})^2}{2\sigma_{s2}^2}\right). \tag{31}$$

This function has five parameters. Thus, we have to optimize all five parameters for fitting. The black dashed line in the first panel of Fig. 7 is the double-lognormal fit to the numerical PDF at $a = 1$. The double-lognormal function fits the numerical PDFs very well, with fit parameters provided in Table 2.

The PDFs for the later times ($a = 0.1$ and 0.01) are shown in the second and third rows of Fig. 7. At these later stages in the contraction of the clouds, the PDFs become close to lognormal. The green dotted lines represent the corresponding lognormal fits
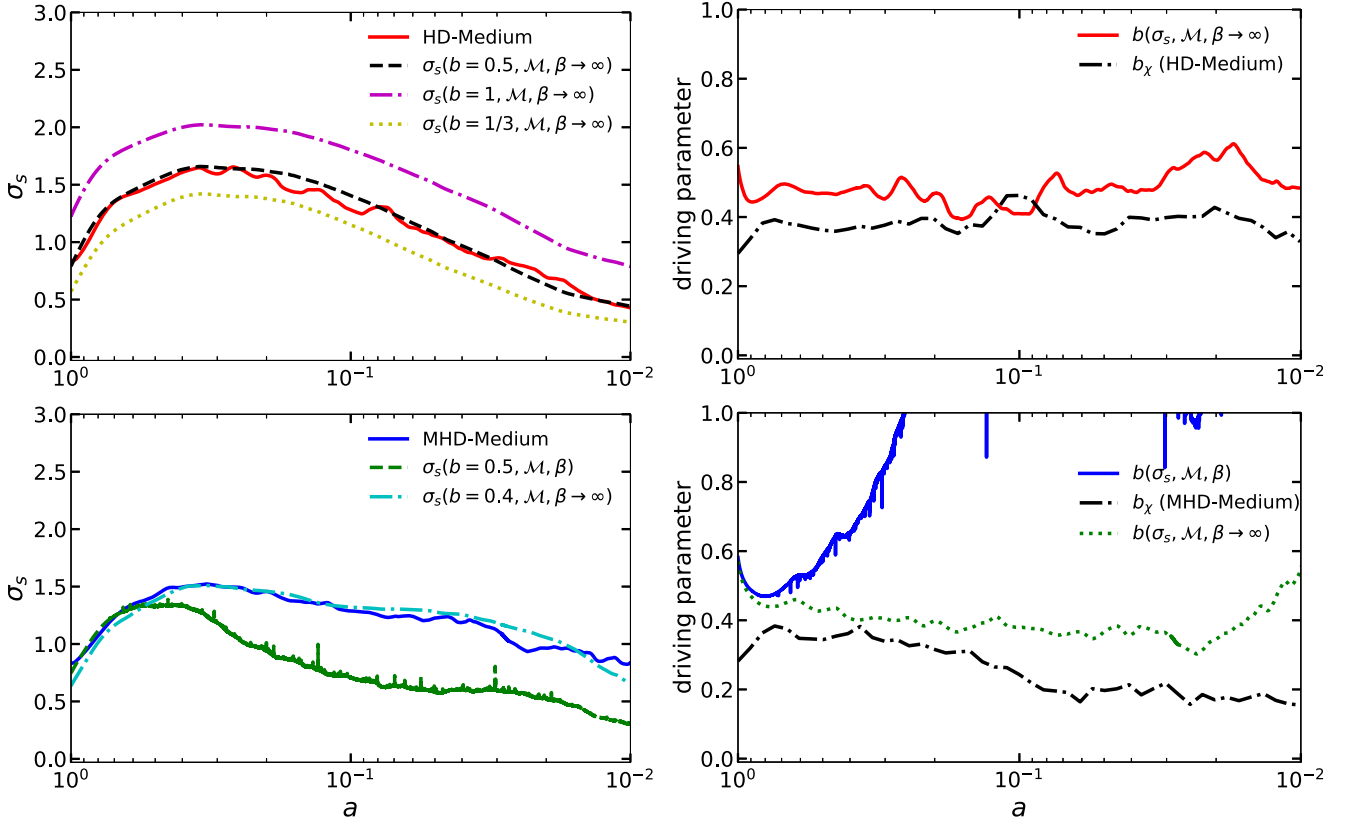
Figure 6. Evolution of standard deviation of log-density (σ_s) (left-hand panels) and driving parameter b and b_χ (right-hand panels) as a function of the scale factor a for HD-Medium (top panels) and MHD-Medium (bottom panels). In the upper-left panel, the red solid line represents the evolution of σ_s for HD simulation and the black dashed line is the corresponding theoretical prediction, equation (24) with $b = 0.5$. The magenta and yellow lines in the upper-left panel correspond to the theoretical predictions for purely solenoidal ($b \sim 1/3$) and purely compressive ($b \sim 1$) driving. The bottom-left panel presents the result for MHD-Medium (blue solid line) and the green line corresponds to the theoretical model, equation (25) with $b = 0.5$. The cyan line in the bottom panel is the HD limit ($\beta \rightarrow \infty$) of the MHD model (equation 25) with $b = 0.4$, which fits the data well. In the upper-right panel, the red solid line corresponds to the evolution of the driving parameter (b) that has been calculated using equation (26) with $\beta \rightarrow \infty$ and the black dashed-dotted line is b_χ calculated using equation (28). In the bottom-right panel, the blue line is b calculated from equation (26) and the black dashed dotted line is b_χ. The green dotted line corresponds to equation (26) with $\beta \rightarrow \infty$.

via equation (29). However, some intermittency and accompanying skewness remains, which is why we also show fits using the Hopkins (2013) intermittency PDF, equation (30) as the blue solid lines (with fit parameters provided in Table 3). These provide very good fits to all the simulations at $a = 0.1$ and 0.01, when the clouds have become fairly dense and reached a nearly isothermal, cold state, which can be seen from the temperature projection plots in Fig. 5.

4 LIMITATIONS

In this section, we discuss some of the main limitations of our work. As a result of the simplicity of hydrodynamic simulations, comparisons with observational results are limited and should be considered carefully. These limitations are listed below:

(i) In this study, we neglect the detailed chemistry of the gas. Throughout the study we consider a mean molecular weight $\mu = 1$. However, in reality, μ changes from about 1.3 in the atomic phase to about 2.3 in the molecular phase. For simplicity, we did not model this change in μ. However, this does not have a significant impact on our general conclusions and would only marginally change our quantitative results. For example, the sound speed would change by a factor $\sim \sqrt{\mu}$, which is significantly less than the differences between our models with different contraction rates.

(ii) The numerical resolution of our simulations is limited. We have performed all the simulations with a resolution of 512^3 grid points. However, we provide a resolution study in Appendix B, which demonstrates reasonable convergence of the integrated quantities shown in Fig. 2.

(iii) In this study, we only consider constant contraction rates (i.e. independent of time or scale factor). While this allows for a simple and clear investigation of the effects of different constant contraction rates, it does not allow us to study the effects of a dynamical change in the contraction rate, which is for example the case for gravitational contraction, where the contraction accelerates over time. Such cases are considered in the previous work by Robertson & Goldreich (2012). However, here we wanted to focus on the effects of heating and cooling without specifying the physical source of the contraction (for example, gravity, shock waves, or cloud–cloud collisions) and chose a constant contraction rate for simplicity. Follow-up work may study cases where the contraction rate is time- and scale-dependent.

5 SUMMARY AND CONCLUSIONS

In this paper, we study the compression of magnetized turbulent gas, incorporating the effects of radiative heating and cooling.
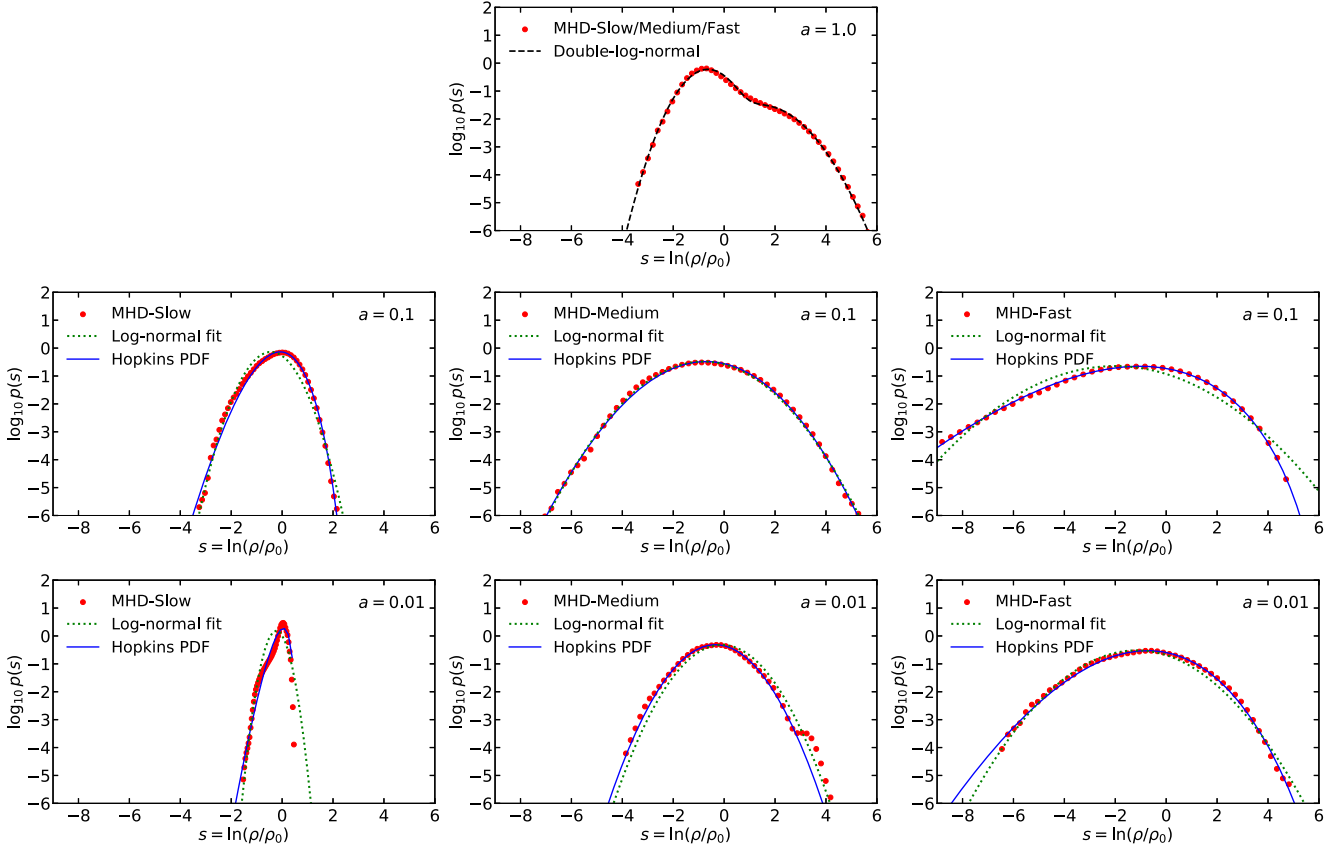
Figure 7. PDFs of logarithmic density contrast $s \equiv \ln(\rho/\rho_0)$ for different contraction models. In the first row, we show the density PDF at $a = 1.0$ (just after the turbulence is fully developed and just before the contraction starts). The second and third row correspond to the density PDFs at $a = 0.1$ and 0.01, for different compression models, respectively. Different columns (from left to right) correspond to MHD-Slow, MHD-Medium, and MHD-Fast. In each panel, the red points are the simulation PDFs. The black dashed line in the first panel is the double-lognormal fit (equation 31) to the numerical PDF at $a = 1.0$. In all subsequent panels, the green dotted lines represent lognormal fits (equation 29) and the blue solid lines show fits with the intermittency PDF model (equation 30).

Table 2. Fitting parameters for the double-lognormal function at $a = 1$.

Model	ω/H	a	N	σ_{s1}	σ_{s2}	s_{01}	s_{02}
MHD-Slow/Medium/Fast	-1.0	1.0	1.670 ± 0.017	0.618 ± 0.006	0.927 ± 0.016	-0.644 ± 0.021	1.423 ± 0.079

Table 3. Statistical measures of the fitting parameters at $a = 0.1$ and 0.01.

Model	ω/H	a	Sim $\sigma_{s,V}$	lognormal $\sigma_{s,V}$	lognormal s_0	Hopkins $\sigma_{s,V}$	Hopkins θ
MHD-Slow	-0.1	0.1	0.833	0.831 ± 0.010	-0.092 ± 0.040	0.823 ± 0.012	0.028 ± 0.011
MHD-Slow	-0.1	0.01	0.191	0.254 ± 0.009	-0.226 ± 0.034	0.221 ± 0.004	0.050 ± 0.002
MHD-Medium	-1.0	0.1	1.278	1.212 ± 0.003	-0.812 ± 0.013	1.212 ± 0.003	0.012 ± 0.002
MHD-Medium	-1.0	0.01	0.833	0.831 ± 0.010	-0.092 ± 0.040	0.823 ± 0.012	0.028 ± 0.011
MHD-Fast	-10.0	0.1	1.778	1.762 ± 0.029	-2.010 ± 0.079	1.807 ± 0.004	0.207 ± 0.002
MHD-Fast	-10.0	0.01	1.392	1.312 ± 0.009	-1.165 ± 0.031	1.346 ± 0.006	0.077 ± 0.003

We investigate whether compression can form MCs from the warm atomic phase, matching observed properties, such as the linewidth–size relation. We use the grid-based code FLASH for our numerical experiments. The simulations follow the global compression of turbulent gas at moderately initial supersonic velocities (each with a velocity of $11.6 \, \text{km s}^{-1}$ for HD simulations and $11.1 \, \text{km s}^{-1}$ for MHD simulations). A total of six simulations were carried out: three different compression rates (Slow, Medium, and Fast), each for HD (no magnetic fields) and MHD

(with magnetic fields). In the following we summarize our main results:

(i) The global compression enhances the turbulent velocity of purely hydrodynamic turbulence, if the compression time-scale ($1/H$) is smaller than the turbulent dissipation time-scale (τ). For cases with compression time-scale less than dissipation time-scale, although the turbulence does not get enhanced, the natural turbulence dissipation gets delayed due to the energy pumping from

global compression. However, compared to HD turbulence, the situation in MHD turbulence is slightly different. In the MHD models the magnetic field stores additional energy, which replenishes some of the kinetic energy that is dissipated.

(ii) Initially, when the temperature is high ($\sim 5000\,\mathrm{K}$), the cooling rate is also high and the gas undergoes rapid radiative cooling. For all the simulations, the temperature saturates around 5–30 K when the density has reached $n \sim 10^6\,\mathrm{cm}^{-3}$.

(iii) When the contraction rate ($|H|$) is high, the cascade of turbulence energy to smaller scales is limited and dissipation becomes inefficient. As a result, the Mach number ($\mathcal{M}$) becomes hypersonic, too large to be compatible with typical values in the Milky Way. On the other hand, when $\omega/|H| \ll 1$, the dissipation dominates and fails to sustain the turbulence. Only if the contraction time-scale is of the order of the turbulence dissipation time-scale, $\mathcal{M}$ remains in the supersonic regime ($\sim$5–10), consistent with the range of observed Mach numbers in typical MCs in the Milky Way.

(iv) Due to rapid radiative cooling the temperature drops. Thus, the Mach number ($\mathcal{M}$) evolution depends on the balance between turbulence dissipation rate and cooling rate. In the molecular regime, the velocity dispersion for the MHD-Medium simulation shows a strong correlation between velocity dispersion and the size of the cloud (L–σ_v scaling relation) and falls between the Larson relation and the B08 relation, and almost follows the S87 relation. By contrast, the linewidth–size relations for slow and fast compression do not fit the observed scaling relations.

(v) It is observationally established that in the high-density regime ($n \gtrsim 10^3\,\mathrm{cm}^{-3}$), the magnetic field strength (B) is correlated with the density of the cloud and proportional to ρ^κ (for low magnetic field strengths, $\kappa \approx 2/3$, and for ambipolar diffusion driven turbulence $\kappa \approx 0.47$). The calculated B–n correlation from the medium compression MHD simulations falls between these two scalings, as the plasma-β, is about 0.1, which means that the magnetic field is dynamically important, also consistent with observations.

(vi) The relation given by equation (24) between logarithmic density variance (σ_s) and Mach number ($\mathcal{M}$) derived for isothermal turbulence is found to be consistent with the theoretical prediction in the HD case for a forcing parameter $b \approx 0.5$. However, it slightly underpredicts σ_s after $a < 0.1$ which means for our model of compression the value of b is slightly higher. This can be explained by the fact that in this model, b is not constant, but rather changes with scale factor as we go from solenoidal driving (the initial stage of contraction) to a mixed driving (mixture of solenoidal and compressive components), i.e. $1/3 < b < 1$. We find that direct computation of the effective driving parameter (b) using equation (26) with $\beta \to \infty$ gives $b \sim 0.4$–0.5, i.e. the turbulence is a mild mixture of compressive components with the initial solenoidal modes. This is also reasonably consistent with the driving parameter (b_χ) computed by Helmholtz decomposition of the velocity field (equation 28). However, for MHD there is a difference between the simulation result and the theoretical prediction (equation 24) when $b \approx 0.5$ is assumed. The evolution of b computed from equation (26) suggests that $b > 1$. This discrepancy is because the Alfvén Mach number ($\mathcal{M}_\mathrm{A}$) drops below 2, which means the magnetic field becomes very strong and the σ_s–$\mathcal{M}$ relation is no longer applicable (Molina et al. 2012). However, the velocity spectra give reasonable values of the driving parameter ($b_\chi \sim$ 0.3–0.4), i.e. the suppression of the compressive modes due to strong magnetic fields leave the turbulence as almost completely solenoidal.

(vii) Just after the turbulence is fully developed and before the contraction starts, which is when a two-phase medium (WMN and CNM) is established, we find that a double-lognormal density PDF provides a good fit to the simulation data. At later times, during the contraction, almost all of the gas becomes dense and cold, such that the isothermal approximation for the density PDF provides a reasonable approximation, and the simulation PDFs are well described by an intermittency PDF model (cf. Fig. 7).

In summary, using idealized simulations, we find that the large-scale compression of the warm, atomic, magnetized ISM can drive turbulence by injecting energy into the system due to compression, if the contraction time-scale is less than the turbulence dissipation time-scale. The models with contraction time-scale similar to dissipation time-scale can reasonably produce key observed physical properties of MCs. There are several candidates for causing such turbulent compression: global gravitational contraction on large scales, compression due to stellar feedback (e.g. supernova shock waves), or cloud–cloud collisions.

REFERENCES

Audit E., Hennebelle P., 2005, A&A, 433, 1
Basu S., 2000, ApJ, 540, L103
Beattie J. R., Federrath C., Klessen R. S., 2019a, MNRAS, 487, 2070
Beattie J. R., Federrath C., Klessen R. S., Schneider N., 2019b, MNRAS, 488, 2493
Beck R., 2015, A&AR, 24, 4
Bernard J.-P. et al., 2008, AJ, 136, 919
Birnboim Y., Federrath C., Krumholz M., 2018, MNRAS, 473, 2144
Bolatto A. D., Leroy A. K., Rosolowsky E., Walter F., Blitz L., 2008, ApJ, 686, 948
Brandenburg A., Subramanian K., 2005, Phys. Rep., 417, 1
Cox D. P., Tucker W. H., 1969, ApJ, 157, 1157
Crutcher R. M., 1999, ApJ, 520, 706
Crutcher R. M., 2012, ARA&A, 50, 29
Crutcher R. M., Roberts D. A., Troland T. H., Goss W. M., 1993, 182, 39.02
Dawson J. R., Ntormousi E., Fukui Y., Hayakawa T., Fierlinger K., 2015, ApJ, 799, 64
Dubrulle B., 1994, Phys. Rev. Lett., 73, 959
Eswaran V., Pope S. B., 1988, Phys. Fluids, 31, 506
Falgarone E., Troland T. H., Crutcher R. M., Paubert G., 2008, A&A, 487, 247
Federrath C., 2013a, MNRAS, 436, 1245

Federrath C., 2013b, MNRAS, 436, 3167
Federrath C., 2016, J. Plasma Phys., 82, 535820601
Federrath C., Banerjee S., 2015a, MNRAS, 448, 3297
Federrath C., Banerjee S., 2015b, MNRAS, 448, 3297
Federrath C., Klessen R. S., 2012, ApJ, 761, 156
Federrath C., Klessen R. S., Schmidt W., 2008, ApJ, 688, L79
Federrath C., Roman-Duval J., Klessen R. S., Schmidt W., Mac Low M. M., 2010, A&A, 512, A81
Federrath C., Chabrier G., Schober J., Banerjee R., Klessen R. S., Schleicher D. R. G., 2011, Phys. Rev. Lett., 107, 114504
Federrath C., Schrön M., Banerjee R., Klessen R. S., 2014, ApJ, 790, 128
Federrath C. et al., 2016, 832, 143
Federrath C. et al., 2017, in Crocker R. M., Longmore S. N., Bicknell G. V., eds, Proc. IAU Symp. 322, The Multi-Messenger Astrophysics of the Galactic Centre. Cambridge University Press, UK, p. 123
Fiedler R. A., Mouschovias T. C., 1993, ApJ, 415, 680
Fryxell B. et al., 2000, ApJS, 131, 273
Gao Y., Solomon P. M., 2004, ApJ, 606, 271
Gazol A., Kim J., 2013, ApJ, 765, 49
Gerrard I. A., Federrath C., Kuruwita R., 2019, MNRAS, 485, 5532
Goldbaum N. J., Krumholz M. R., Matzner C. D., McKee C. F., 2011, ApJ, 738, 101
Gratier P., Braine J., Rodriguez-Fernandez N. J., Israel F. P., Schuster K. F., Brouillet N., Gardan E., 2010, A&A, 512, A68
Han J., 2017, ARA&A, 55, 111
Hennebelle P., Audit E., 2007, A&A, 465, 431
Heyer M. H., Brunt C. M., 2004, ApJ, 615, L45
Heyer M., Dame T., 2015, ARA&A, 53, 583
Hopkins P. F., 2013, MNRAS, 430, 1880
Hughes A. et al., 2010, MNRAS, 406, 2065
Jameson K. E. et al., 2019, ApJS, 244, 7
Jin K., Salim D. M., Federrath C., Tasker E. J., Habe A., Kainulainen J. T., 2017, MNRAS, 469, 383
Kazantsev A. P., 1968, Sov. J. Exp. Theor. Phys., 26, 1031
Klessen R. S., Hennebelle P., 2010, A&A, 520, A17
Körtgen B., Seifried D., Banerjee R., Vázquez-Semadeni E., Zamora-Avilés M., 2016, MNRAS, 459, 3460
Körtgen B., Federrath C., Banerjee R., 2017, MNRAS, 472, 2496
Körtgen B., Federrath C., Banerjee R., 2019, MNRAS, 482, 5233
Kowal G., Lazarian A., Beresnyak A., 2007, ApJ, 658, 423
Koyama H., Inutsuka S.-i., 2002, ApJ, 564, L97
Kritsuk A. G., Norman M. L., 2002, ApJ, 569, L127
Kritsuk A. G., Padoan P., Wagner R., Norman M. L., 2007, in Shaikh D., Zank G. P., eds, AIP Conf. Proc. Vol. 932, Turbulence and Nonlinear Processes in Astrophysical Plasmas. Am. Inst. Phys., New York, p. 393
Kritsuk A. G., Ustyugov S. D., Norman M. L., 2017, New J. Phys., 19, 065003
Krumholz M. R., Federrath C., 2019, Front. Astron. Space Sci., 6, 7
Krumholz M. R., Matzner C. D., McKee C. F., 2006, ApJ, 653, 361
Larson R. B., 1981, MNRAS, 194, 809
Larson R. B., 2005, MNRAS, 359, 211
Lee Y.-N., Hennebelle P., 2016, A&A, 591, A30
Li Y., Klessen R. S., Mac Low M.-M., 2003, ApJ, 592, 975
Li Z.-Y., Nakamura F., 2006, ApJ, 640, L187
Mac Low M.-M., 1999, ApJ, 524, 169
Mac Low M.-M., Klessen R. S., 2004, Rev. Mod. Phys., 76, 125
Mac Low M.-M., Klessen R. S., Burkert A., Smith M. D., 1998, Phys. Rev. Lett., 80, 2754
Matzner C. D., 2002, ApJ, 566, 302
McKee C. F., Ostriker E. C., 2007, ARA&A, 45, 565
Mocz P., Burkhart B., Hernquist L., McKee C. F., Springel V., 2017, ApJ, 838, 40
Molina F. Z., Glover S. C. O., Federrath C., Klessen R. S., 2012, MNRAS, 423, 2680

Ntormousi E., Burkert A., Fierlinger K., Heitsch F., 2011, ApJ, 731, 13
Ossenkopf V., Mac Low M. M., 2002, A&A, 390, 307
Padoan P., Nordlund Å., 1999, ApJ, 526, 279
Padoan P., Nordlund Å., 2011, ApJ, 730, 40
Padoan P., Nordlund A., Jones B. J. T., 1997a, MNRAS, 288, 145
Padoan P., Jones B. J. T., Nordlund Å. P., 1997b, ApJ, 474, 730
Padoan P. et al., 2014, in Beuther H., Klessen R. S., Dullemond C. P., Henning T., eds, Protostars and Planets VI, University of Arizona Press, Baltimore, Maryland, USA. p. 77
Padoan P., Pan L., Haugbølle T., Nordlund Å., 2016a, ApJ, 822, 11
Padoan P., Juvela M., Pan L., Haugbølle T., Nordlund Å., 2016b, ApJ, 826, 140
Padoan P., Haugbølle T., Nordlund Å., Frimann S., 2017, ApJ, 840, 48
Pan L., Padoan P., Haugbølle T., Nordlund Å., 2016a, ApJ, 825, 30
Pan L., Padoan P., Haugbølle T., Nordlund Å., 2016b, ApJ, 825, 30
Passot T., Vázquez-Semadeni E., 1998, Phys. Rev. E, 58, 4501
Planck Collaboration XXXV, 2016, A&A, 586, A138
Price D. J., Federrath C., 2010, MNRAS, 406, 1659
Raymond J. C., Cox D. P., Smith B. W., 1976, ApJ, 204, 290
Robertson B., Goldreich P., 2012, ApJ, 750, L31
Roman-Duval J., Federrath C., Brunt C., Heyer M., Jackson J., Klessen R. S., 2011, ApJ, 740, 120
Salim D. M., Federrath C., Kewley L. J., 2015, ApJ, 806, L36
Schleicher D. R. G., Schober J., Federrath C., Bovino S., Schmidt W., 2013, New J. Phys., 15, 023017
Schmidt W., Federrath C., Hupp M., Kern S., Niemeyer J. C., 2009, A&A, 494, 127
Schober J., Schleicher D., Federrath C., Glover S., Klessen R. S., Banerjee R., 2012, ApJ, 754, 99
Seifried D., Banerjee R., Klessen R. S., Duffin D., Pudritz R. E., 2011, MNRAS, 417, 1054
Sharda P., Federrath C., da Cunha E., Swinbank A. M., Dye S., 2018, MNRAS, 477, 4380
Sharda P. et al., 2019, MNRAS, 487, 4305
She Z.-S., Waymire E. C., 1995, Phys. Rev. Lett., 74, 262
Shull J. M., van Steenberg M., 1982, ApJS, 48, 95
Solomon P. M., Rivolo A. R., Barrett J., Yahil A., 1987, ApJ, 319, 730
Sur S., Federrath C., Schleicher D. R. G., Banerjee R., Klessen R. S., 2012, MNRAS, 423, 3148
Sutherland R. S., Dopita M. A., 1993, ApJS, 88, 253
Tremblin P. et al., 2014, A&A, 564, A106
Vazquez-Semadeni E., 1994, ApJ, 423, 681
Vázquez-Semadeni E., Ballesteros-Paredes J., Klessen R. S., 2003, ApJ, 585, L131
Vázquez-Semadeni E., Gómez G. C., Jappsen A. K., Ballesteros-Paredes J., González R. F., Klessen R. S., 2007, ApJ, 657, 870
Vázquez-Semadeni E., Colín P., Gómez G. C., Ballesteros-Paredes J., Watson A. W., 2010, ApJ, 715, 1302
Vlemmings W. H. T., van Langevelde H. J., 2007, A&A, 472, 547
Waagan K., Federrath C., Klingenberg C., 2011, J. Comput. Phys., 230, 3331
Wada K., Norman C. A., 2001, ApJ, 547, 172
Wang P., Li Z.-Y., Abel T., Nakamura F., 2010, ApJ, 709, 27
Watson W. D., 2009, 36, 113
Wilson C. D., Walker C. E., Thornley M. D., 1997, ApJ, 483, 210
Wong T., Blitz L., 2002, ApJ, 569, 157
Zuckerman B., Evans N. J., II, 1974, ApJ, 192, L149

APPENDIX A: MORPHOLOGY OF HD-FLOW FOR MEDIUM COMPRESSION

Fig. A1 shows the flow morphology for the hydrodynamic (HD) simulation with medium compression, similar to the MHD simulation with medium compression shown in Fig. 5.
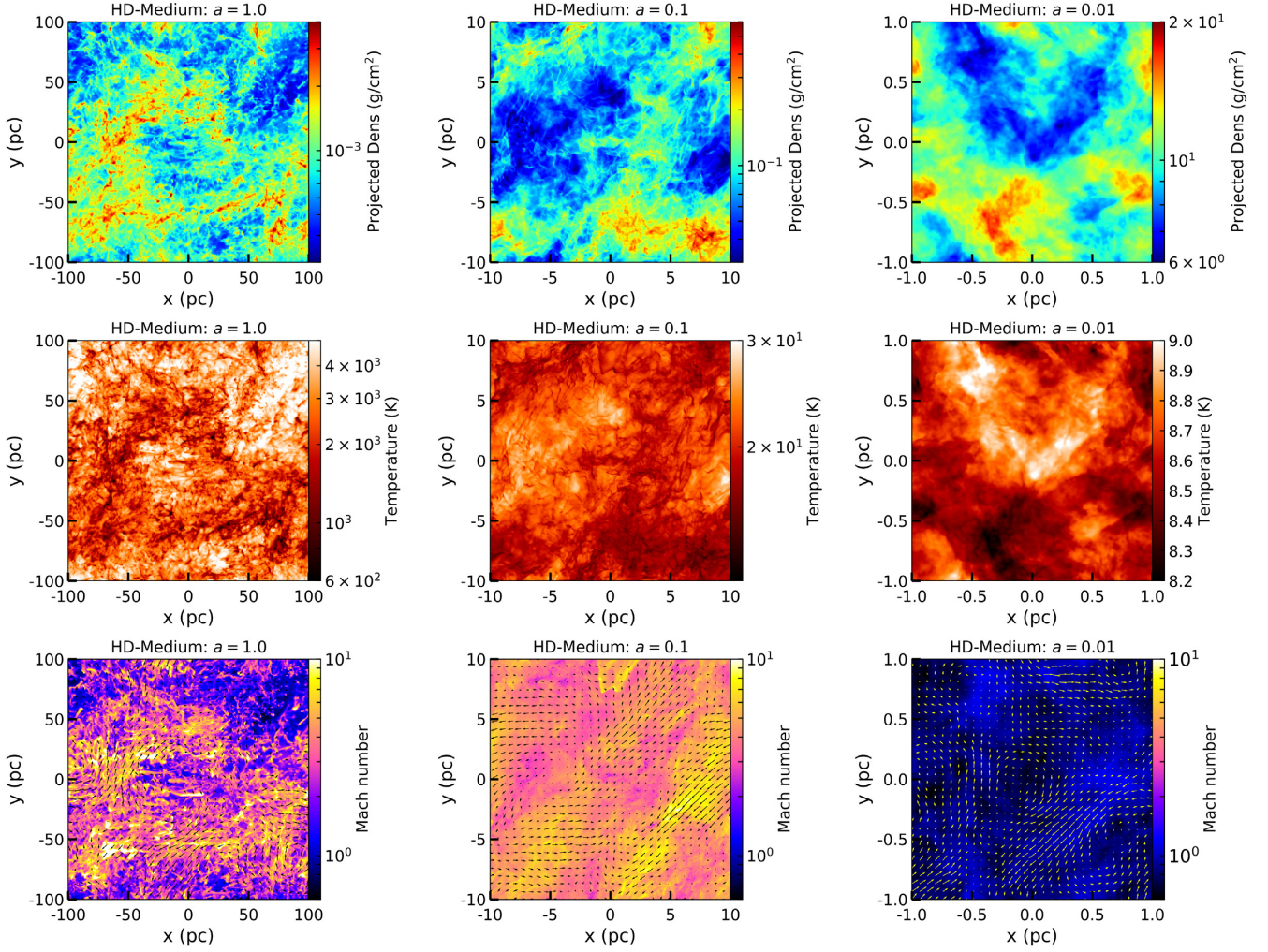
Figure A1. Same as Fig. 5, but for the HD-Medium simulation.

APPENDIX B: CONVERGENCE WITH NUMERICAL GRID RESOLUTION

In Fig. B1, we show the dependence and convergence of our numerical results with grid resolution. Fig. B1 shows the same integrated quantities as Fig. 2 for the MHD-Medium compression ($\omega/H = -1$) model, but at different numerical resolutions. We perform three different simulations with grid resolutions of 128^3 (black line), 256^3 (green line), and 512^3 (blue line). The first panel shows that the variations of temperature with different resolutions are almost negligible when the cloud becomes cold and dense. For the velocity dispersion (second panel of Fig. B1), we see some dependence on numerical resolution, however, there is no clear trend for this dependence. Thus, our end results do not systematically depend on resolution. A similar trend can be seen for the mass-weighted Mach number (third panel of Fig. B1). The quantities that show the strongest resolution dependence involve the magnetic field. As the dynamo amplification and the level of saturation of turbulent dynamo depend on high Reynolds number, which is a resolution-dependent quantity, and the tangling of magnetic field

requires higher resolution to resolve, higher grid resolution would produce more converged results. We can clearly see this behaviour in the magnetic field (fourth panel), plasma β (fifth panel), and Alfvén Mach number (sixth panel).

We note that the fluctuations in plasma β and Alfvén Mach number are of physical origin. These variables are bursty, because of how they are defined. The bursts come from local fluctuations of thermal and magnetic pressure. Since these can vary substantially on small scales, even the space-averages still show them. For example, if there is just one cell or a small local region that has tiny magnetic pressure, then β and $\mathcal{M}_A$ will shoot up (in extreme cases, they might temporarily approach values near infinity, if the magnetic pressure goes to zero in a local region).

Overall, we find that a grid resolution of 128^3 cells is not enough for simulating the compression of supersonic, magnetized turbulent gas in the context of MC formation. We need at least a grid resolution of 256^3 for this study to achieve convergence to within a factor of ~ 2 at all a. We conclude that for our standard resolution of 512^3 we obtain reasonable, nearly converged results for the integrated cloud quantities that we have focused on in this study.
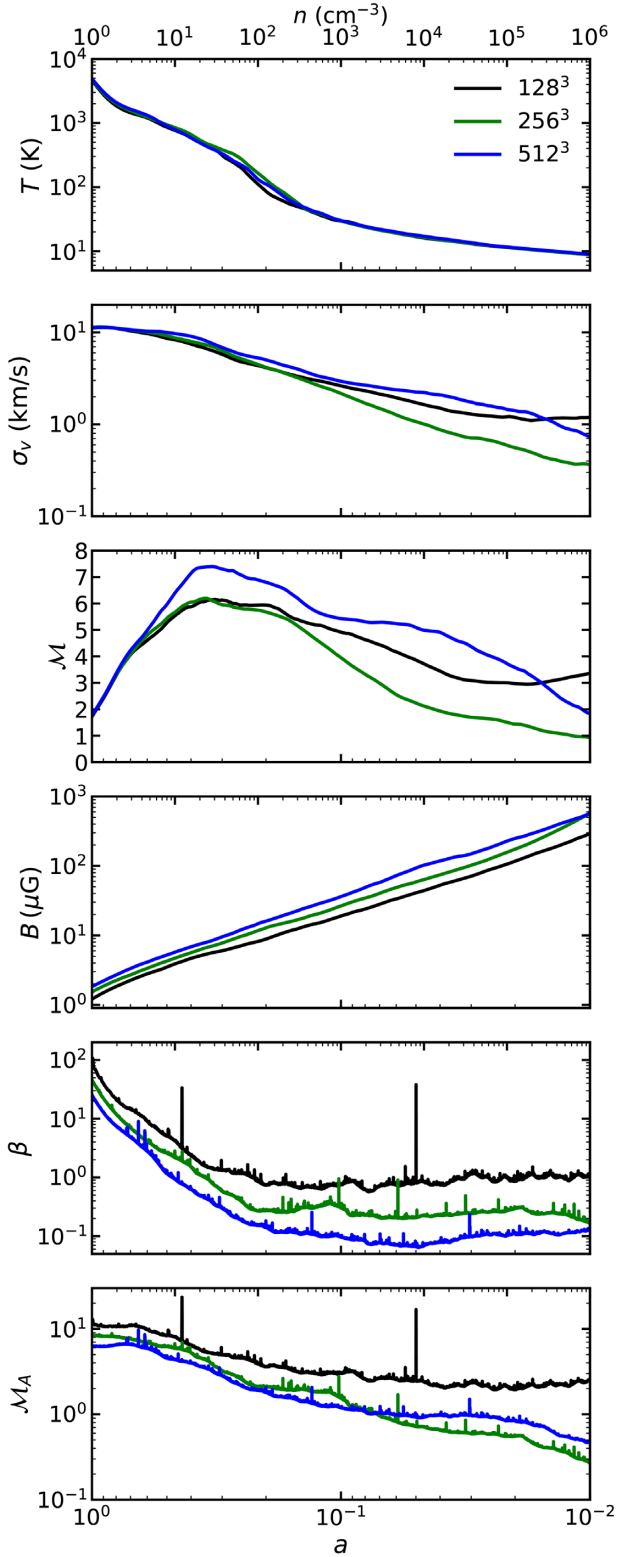
Figure B1. Convergence study of integrated quantities with numerical grid resolution for the MHD-Medium compression ($\omega/H = -1$) model. In each panel, we show results from three different simulations with grid resolutions of 128^3 (black), 256^3 (green), and 512^3 (blue) cells.

This paper has been typeset from a TEX/LATEX file prepared by the author.